Precise Modeling of Inductive Wireless Power Transfer With Lossy Magnetic Sheets

Do–Hyeon Kim

***Abstract*—Accurately analyzing power losses in inductive wireless power transfer (WPT) including lossy magnetic sheet is challenging, as coils have mutual influences on each other's power dissipation. This article proposes a precise analytic model for inductive WPT with lossy magnetic sheets. Combining a partial element equivalent circuit (PEEC) with a two–port network, both self– and mutual-impedances of coupled coils are accurately calculated considering eddy current effects. Furthermore, the proposed PEEC–based model incorporates the complex permeabilities of lossy magnetic sheets, thus addressing a critical gap in previous studies that have not considered magnetic sheets with losses in their analysis. The suggested model is verified with finite element method (FEM) simulations and measurements. Compared with an FEM simulator, the proposed model calculates impedances about 31 times faster, substantially reducing the number of meshes. Finally, the ohmic and magnetic losses in coil windings and magnetic sheets are investigated with the proposed model, demonstrating that the phase adjustment of currents using the compensation capacitor is effective to reduce the losses caused by eddy currents and lossy magnetic sheets. The proposed model offers more detailed and accurate loss analysis, compared to conventional methods based on circuit analysis.**

***Index Terms*—Eddy current, inductance, magnetic materials, modeling, partial element equivalent circuit (PEEC), resistance, wireless power transfer (WPT).**

I. INTRODUCTION

NOWADAYS, inductive wireless power transfer (WPT) is increasingly being used in a variety of applications, such as medical implants, mobiles, and electric vehicles [1], [2], [3], [4], [5], [6], [7]. Notably, recent mobile devices support wireless charging for enhanced user convenience. In general, a mobile device based on Qi standard [1] is closely positioned on a power transmitter to achieve a sufficient coupling coefficient for efficient power delivery. In addition, magnetic shielding sheets, like ferrite or nanocrystal sheets, are incorporated to enhance the inductive coupling between transmitter (Tx) and receiver (Rx) coils, as well as to protect the device from magnetic fields.

Given that most power loss occurs within coils, predicting coil loss using an analytic model is essential to design WPT systems. However, the loss analysis of coupled coils presents tough challenges due to mutual interactions between coils. Closely adjacent coils significantly influence power dissipation within each other through eddy currents [7], [8], [9], [10], [11]. These challenges are further exacerbated when lossy magnetic sheets are introduced.

Various methods have been presented for designing and analyzing coils [11], [12], [13], [14], [15], [16], [17], [18]. The self– and mutual inductances are calculated considering magnetic sheets [13], [14]. By applying boundary conditions, complex permeabilities of lossy magnetic sheets are incorporated into the calculations. However, these calculations do not account for current crowding due to eddy currents, like skin effect or proximity effect. As the intricate current distributions within conductors are not considered in [13] and [14], these methods are not able to estimate ac resistance or losses in coils accurately at high frequencies.

A partial element equivalent circuit (PEEC) is used to capture skin and proximity effects in coils [15], [16]. Both inductance and resistance can be calculated accurately by considering eddy currents with a PEEC model. In particular, the study of [16] examines the self– and mutual impedances of coupled coils with the consideration of the dielectric loss, yet it has not included magnetic sheets in its analysis.

The loss of a single coil on a magnetic sheet has been investigated [17], [18]. For analytical simplicity, the magnetic sheet is substituted with imaginary current sources, based on image theory. In addition, the coupling proximity losses in two coupled coils with magnetic sheets are studied in [11]. In these references, magnetic sheets are commonly assumed to be lossless to simplify the analysis. Consequently, these studies primarily focus on ohmic losses within windings, excluding magnetic losses.

This article proposes a precise analytic model for inductively coupled coils with lossy magnetic sheets. A PEEC is combined with a two–port network to model coupled coils, which enables to analyze not only the self–impedance of each coil but also mutual impedance between coils considering eddy current effects within conductors. In addition, this article introduces a method to incorporate the effects of lossy magnetic sheets into a PEEC model, in contrast to previous studies that were conducted without magnetic sheets or with the assumption of lossless sheets. In this way, the proposed analytical model can reflect the mutual interaction between coupled coils taking into account both eddy current and lossy magnetic sheets, which has not been addressed in previous studies. Table I compares this work with previous studies.

Manuscript received 29 January 2024; revised 22 May 2024; accepted 14 June 2024. Date of publication 19 June 2024; date of current version 16 July 2024. This work was supported by the U.S. Department of Commerce under Grant 123456. Recommended for publication by Associate Editor J. Acero.

The author is with the Samsung Electronics, Suwon 16677, South Korea (e-mail: dh0104.kim@samsung.com).

Color versions of one or more figures in this article are available at https://doi.org/10.1109/TPEL.2024.3416832.

Digital Object Identifier 10.1109/TPEL.2024.3416832

TABLE I
COMPARISON WITH PREVIOUS STUDIES

	Impedance calculation	Skin and proximity effects	Magnetic sheet	Supporting coupled coils
This work	Inductance and resistance	Considered	Lossy sheet	O
[11]	Resistance only	Considered	Lossless sheet only	O
[13], [14]	Inductance only (No AC resistance)	Not considered	Lossy sheet	O
[16]	Inductance and resistance	Considered	Not included	O
[17]	Inductance and resistance	Considered	Lossless sheet only	X (Single coil only)
[18]	Resistance only	Considered	Lossless sheet only	X (Single coil only)

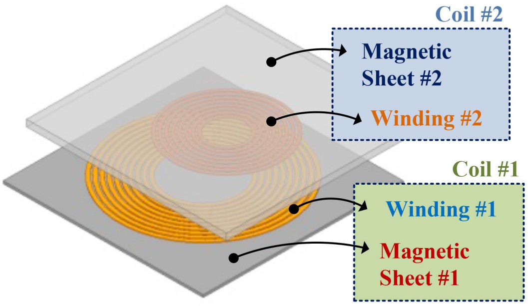

Fig. 1. Illustration of coil #1 and coil #2.

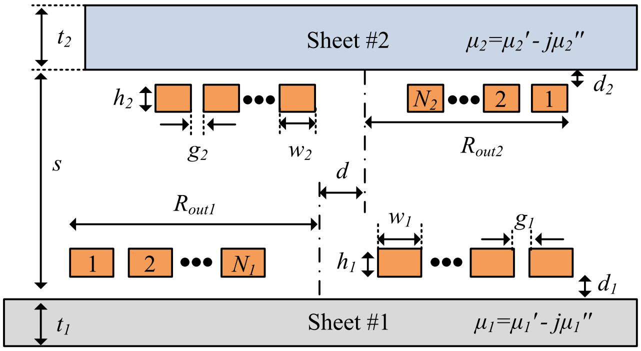

Fig. 2. Cross-sectional view of coil #1 and coil #2.

The rest of this article is organized as follows. Section II introduces the PEEC–based model for coupled coils with lossy magnetic sheets. Section III verifies the proposed model with finite element method (FEM) simulations and measurements. Loss analysis results obtained with the proposed model are presented in Section IV. Finally, Section V concludes this article.

II. PEEC–BASED MODEL FOR COUPLED COILS

For two coupled coils, a PEEC is integrated with a two–port network in this article. However, it can be expanded to multiple coils with a multiport network. The PEEC modeling procedure consists of two steps: discretization and construction of an equivalent circuit, both of which are explained in this section. Then, the procedure for calculating coil impedance based on the equivalent circuit will be introduced.

A. Discretization

In Fig. 1, Winding #1 and Winding #2 are depicted as circular spirals with rectangular cross sections. Spiral windings can be substituted with serially connected multiple circular loops for analysis [12], [15]. The cross-sectional view of the windings and magnetic sheets is illustrated in Fig. 2, where the geometric parameters are defined. Multiple loops are discretized with circular volumetric filamentary loops, using a two-dimensional (2-D) meshing operation as shown in Fig. 3. The size of a mesh should be chosen to be less than skin depth to accurately capture current distributions within windings [15].

B. Construction of an Equivalent Circuit

Winding #1 and Winding #2 can be conceptualized as an assembly of interconnected volumetric filamentary loops. Fig. 4 shows the constructed equivalent circuit of these volumetric filamentary loops. The total number of volumetric filamentary loops is denoted by $N_T = N_{T1} + N_{T2}$, where $N_{T1} = m \times N_1$ and $N_{T2} = n \times N_2$, with m and n representing the number of meshes for a single loop of Winding #1 and Winding #2, respectively. N_1 and N_2 are the turn numbers of windings, as shown in Fig. 2. Winding #1 and Winding #2 are replaced with multiple loops, numbered from 1 to $(N_1 + N_2)$ in Fig. 3.

Each impedance branch in Fig. 4 corresponds to a single volumetric filamentary loop. The self–impedance of the gth volumetric filamentary loop is denoted as z_g, which consists of resistance and inductance, R_g and L_g, respectively. Unlike the PEECs presented in [15], [16], and [18], R_g is composed of two components: $R_{g.\mathrm{mag}}$, representing the resistance corresponding to the magnetic losses of sheets, and $R_{g.\mathrm{ohm}}$, which accounts for the ohmic loss in the gth volumetric filamentary loop. Similarly, L_g includes $L_{g.\mathrm{mag}}$, representing the additional inductance caused by magnetic sheets, while $L_{g.\mathrm{air}}$ indicates the inductance in the absence of magnetic sheets.

Branches connected in parallel represent a single loop among multiple loops. Because each loop of multiple loops is composed of a volumetric filamentary loop connected in parallel. For example, the pth loop includes m parallel branches in the equivalent circuit for $1 \leq p \leq N_1$, as shown in Fig. 4. For $(N_1 + 1) \leq p \leq (N_1 + N_2)$, the pth loop consists of n branches like the qth loop. All branches are coupled with mutual impedances (only mutual impedance between the gth and the lth volumetric filamentary loops, z_{gl}, is shown for simplicity), leading skin and proximity effects [15], [16]. With the presence of lossy magnetic sheets, z_{gl} has a resistive element, R_{gl}, indicating mutual resistance. Mutual resistances between volumetric filamentary

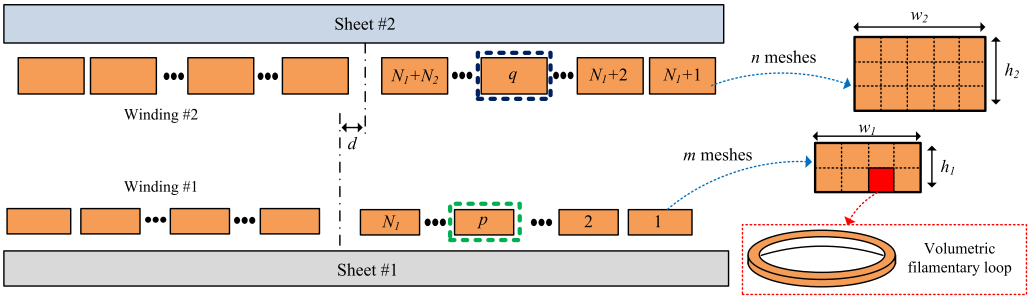

Fig. 3. Discretization of multiple loops into volumetric filamentary loops.

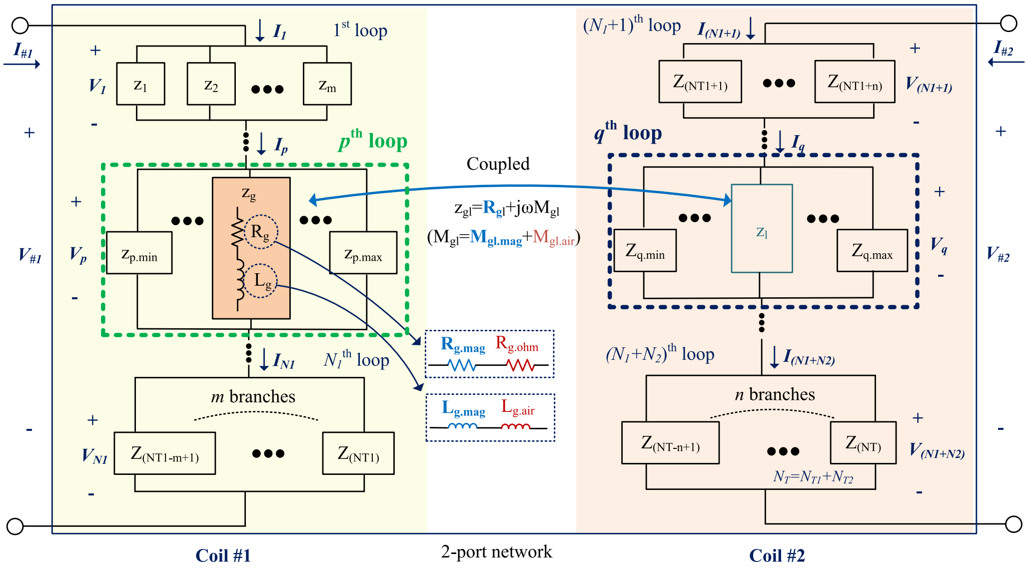

Fig. 4. Equivalent circuit of interconnected volumetric filamentary loops.

loops are caused by magnetic losses in Sheet #1 and Sheet #2, as meshes are less than skin depth and mutual influences between volumetric filamentary loops via eddy currents are negligible. By incorporating $R_{g.\mathrm{mag}}$ and R_{gl}, which are the resistances due to magnetic losses, into the equivalent circuit, loss factors of magnetic sheets (μ_1'' and μ_2'') can be included in the analysis. Similarly, $L_{g.\mathrm{mag}}$ and $M_{gl.\mathrm{mag}}$ in Fig. 4 account for the contribution of μ_1' and μ_2' to self- and mutual inductances, respectively, with further details to be discussed later.

C. Derivation of Coil Impedances

Coil #1 and Coil #2 compose a two-port network in Fig. 4. According to the definition of Z–parameters, and similar to the approach in [15], Z_{11} and Z_{21} can be derived from the voltages across Coil #1 and Coil #2, $V_{\#1}$ and $V_{\#2}$, respectively, when $I_{\#1}$ is set to1 A and $I_{\#2}$ to 0 A. Here, $I_{\#1}$ and $I_{\#2}$ represent the currents of Coil #1 and Coil #2, respectively. Then, with $I_{\#1}$ of 1 A and $I_{\#2}$ of 0 A, Z_{11} and Z_{21} are given by

$$Z_{11} = V_{\#1} = \sum_{p=1}^{N_1} V_p \tag{1}$$

$$Z_{21} = V_{\#2} = \sum_{p=N_1+1}^{N_2} V_p \tag{2}$$

where V_p indicates the voltage across the pth loop of $(N_1 + N_2)$ loops. The current that flows through the pth loop is denoted as I_p, which is equal to $I_{\#1}$ and $I_{\#2}$ for $1 \le p \le N_1$ and $(N_1 + 1) \le p \le (N_1 + N_2)$, respectively. Then, V_p is derived from (3)

$$\boldsymbol{V_L} = \begin{bmatrix} Y_{11} & Y_{12} & \cdots & Y_{1(N_1+N_2)} \\ Y_{21} & Y_{22} & \cdots & Y_{2(N_1+N_2)} \\ \vdots & \vdots & \ddots & \vdots \\ Y_{(N_1+N_2)1} & Y_{(N_1+N_2)2} & \cdots & Y_{(N_1+N_2)(N_1+N_2)} \end{bmatrix}^{-1} \boldsymbol{I_L} \tag{3}$$

where

$$\boldsymbol{V_L} = \begin{bmatrix} V_1 & \cdots & V_{(N_1)} & V_{(N_1+1)} & \cdots & V_{(N_1+N_2)} \end{bmatrix}^T, \tag{4}$$

$$\boldsymbol{I_L} = \begin{bmatrix} I_1 & \cdots & I_{(N_1)} & I_{(N_1+1)} & \cdots & I_{(N_1+N_2)} \end{bmatrix}^T. \tag{5}$$

The matrix of (3) is composed of the admittances of multiple loops. The element of the pth row and qth column, denoted as

Y_{pq}, represents the admittance between the pth loop and the qth loop ($p, q = 1, 2, \ldots, (N_1 + N_2)$). Y_{pq} is calculated by summing the self- and mutual admittances of the volumetric filamentary loops, which compose the pth loop and the qth loop

$$Y_{pq} = \sum_{i=p_{.\min}}^{i=p_{.\max}} \sum_{j=q_{.\min}}^{j=q_{.\max}} y_{ij} \tag{6}$$

where

$$p_{.\max} = \begin{cases} p \times m, \ \text{for } 1 \le p \le N_1 \\ (p - N_1) \times n + N_{T1}, \ \text{for } N_1 + 1 \le p \le N_1 + N_2 \end{cases} \tag{7}$$

$$p_{.\min} = \begin{cases} (p - 1) \times m + 1, \ \text{for } 1 \le p \le N_1 \\ (p - N_1 - 1) \times n + N_{T1} + 1, \ \text{for } N_1 + 1 \le p \le N_1 + N_2 \end{cases} \tag{8}$$

$$q_{.\max} = \begin{cases} q \times m, \ \text{for } 1 \le q \le N_1 \\ (q - N_1) \times n + N_{T1}, \ \text{for } N_1 + 1 \le q \le N_1 + N_2 \end{cases} \tag{9}$$

$$q_{.\min} = \begin{cases} (q - 1) \times m + 1, \ \text{for } 1 \le q \le N_1 \\ (q - N_1 - 1) \times n + N_{T1} + 1, \ \text{for } N_1 + 1 \le q \le N_1 + N_2 \end{cases}. \tag{10}$$

For instance, when $1 \le p \le N_1$ and $(N_1 + 1) \le q \le (N_1 + N_2)$, as shown in Fig. 4, m volumetric filamentary loops from the ($p_{.\min}$)th to the ($p_{.\max}$)th belong to the pth loop, where $p_{.\min} = (p\text{-}1) \times m + 1$ and $p_{.\max} = p \times m$. Similarly, there are n volumetric filamentary loops in the qth loop from the ($q_{.\min}$)th to the ($q_{.\max}$)th, where $q_{.\min} = (q\text{-}N_1\text{-}1) \times n + N_{T1} + 1$ and $q_{.\max} = (q\text{-}N_1) \times n + N_{T1}$.

In (6), y_{ij} represents the element of the ith row and the jth column in the admittance matrix of volumetric filamentary loops, $\boldsymbol{Y_f}$.

$$\boldsymbol{I_f} = \boldsymbol{Y_f}\,\boldsymbol{V_f} \tag{11}$$

where

$$\boldsymbol{Y_f} = \boldsymbol{Z_f}^{-1} = \begin{bmatrix} z_{11} & z_{12} & \cdots & z_{1(N_T)} \\ z_{21} & z_2 & \cdots & z_{2(N_T)} \\ \vdots & \vdots & \ddots & \vdots \\ z_{(N_T)1} & z_{(N_T)2} & \cdots & z_{(N_T)(N_T)} \end{bmatrix}^{-1} \tag{12}$$

$$\boldsymbol{V_f} = \begin{bmatrix} v_1 & v_2 & \cdots & v_{(N_T)} \end{bmatrix}^T \tag{13}$$

$$\boldsymbol{I_f} = \begin{bmatrix} i_1 & i_2 & \cdots & i_{(N_T)} \end{bmatrix}^T . \tag{14}$$

In (13) and (14), v_g and i_g are the voltage and current of the gth volumetric filamentary loop, respectively. $[\bullet]^T$ represents the transpose matrix of $[\bullet]$. $\boldsymbol{Z_f}$ is the matrix consisting of self- and mutual impedances of volumetric filamentary loops. Diagonal elements represent self-impedances ($z_1, z_2, \ldots, z_{NT}$), while others indicate mutual impedances.

Likewise, Z_{12} and Z_{22} are given by

$$Z_{12} = V_{\#1} = \sum_{k=1}^{N_1} V_k \tag{15}$$

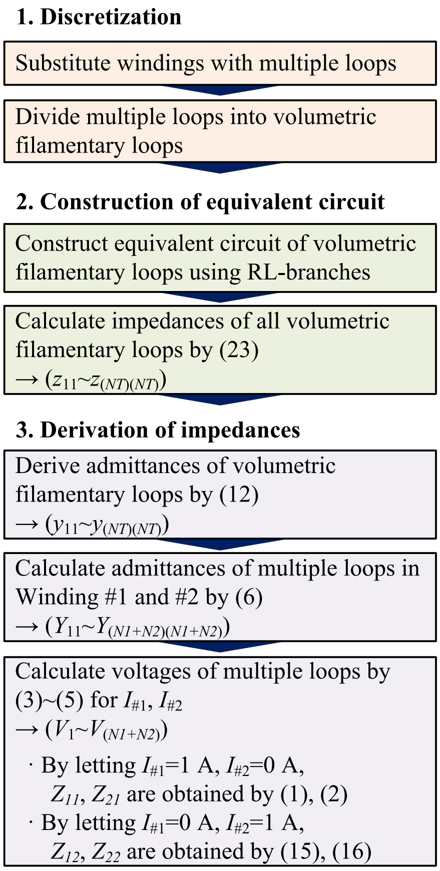

Fig. 5. Procedure of the impedance calculation.

$$Z_{22} = V_{\#2} = \sum_{k=N_1+1}^{N_1+N_2} V_k \tag{16}$$

where V_k is derived in (3) with $I_{\#1}$ set to 0 A and $I_{\#2}$ set to 1 A. Fig. 5 summarizes the procedure of the proposed impedance calculation method.

The inductance and resistance of Coil #1 and Coil #2 are obtained from Z_{11}, Z_{12}, Z_{21}, and Z_{22}.

$$L_{\#1} = \text{imag}\{Z_{11}/\omega\} \tag{17}$$

$$L_{\#2} = \text{imag}\{Z_{22}/\omega\} \tag{18}$$

$$M = \text{imag}\{Z_{12}/\omega\} = \text{imag}\{Z_{21}/\omega\} \tag{19}$$

$$R_{\#1} = \text{real}\{Z_{11}\} \tag{20}$$

$$R_{\#2} = \text{real}\{Z_{22}\} \tag{21}$$

$$R_M = \text{real}\{Z_{12}\} = \text{real}\{Z_{21}\} \tag{22}$$

where imag$\{\bullet\}$ and real$\{\bullet\}$ indicate the imaginary and real parts of ($\bullet$), respectively, with ω representing the angular frequency. $L_{\#1}$, $R_{\#1}$, $L_{\#2}$, and $R_{\#2}$ refer to the self-inductance and resistance of Coil #1 and Coil #2, while M and R_M denote mutual inductance and resistance, respectively.

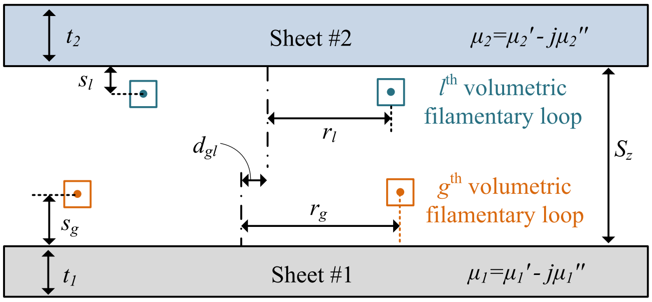

Fig. 6. Cross-sectional view of two volumetric filamentary loops.

D. Impedances of Volumetric Filamentary Loops

Fig. 6 shows a cross-sectional view of the gth and the lth volumetric filamentary loops. The mesh size is so small that volumetric filamentary loops can be approximated as volumeless filamentary loops for mutual impedance calculation [15]. For simple calculations, Sheet #1 and Sheet#2 can be assumed to be infinite in the radial direction [13], [14]. Then, following the method presented in [13] and [14], the mutual impedance between these volumetric filamentary loops, z_{gl}, is followed as

$$z_{gl} = z_{gl.\text{air}} + z_{gl.\text{mag}} \tag{23}$$

where $z_{gl.\text{air}}$ is the mutual impedance that would be with the absence of magnetic sheets, while $z_{gl.\text{mag}}$ represents the additional impedance contributed by magnetic sheets

$$\begin{aligned} z_{gl.\text{air}} = j\omega\mu_0\, r_g r_l \int_0^\infty \int_0^\pi \frac{r_l - d_{gl}\cos\phi}{D} J_1(kr_g)\, J_1(kR) \\ \times\, e^{-k|S_z - s_g - s_l|} d\phi dk \end{aligned} \tag{24}$$

$$\begin{aligned} z_{gl.\text{mag}} = j\omega\mu_0 \pi r_g r_l \int_0^\infty \int_0^\pi \frac{r_l - d_{gl}\cos\phi}{D} J_1(kr_g)\, J_1(kR) \\ \times \left[f(\lambda) + g(\lambda)\right] d\phi dk \end{aligned} \tag{25}$$

where

$$D = \sqrt{r_l^2 + d_{gl}^2 - 2r_l d_{gl}\cos\phi}\,. \tag{26}$$

$J_1(x)$ is the first kind of Bessel function, and μ_0 is the permeability of free space ($4\pi \times 10^{-7}$ H/m). In (25), $f(\lambda)$ and $g(\lambda)$ are defined as

$$f(\lambda) = \frac{\lambda_1 e^{-k(S_z + s_g - s_l)} + \lambda_2 e^{-k(S_z - s_g + s_l)}}{1 - \lambda_1\lambda_2 e^{-2kS_z}} \tag{27}$$

$$g(\lambda) = \frac{2\lambda_1\lambda_2 e^{-2kS_z}\cosh\left[k\left(S_z - s_g - s_l\right)\right]}{1 - \lambda_1\lambda_2 e^{-2kS_z}} \tag{28}$$

where

$$\lambda_1 = \frac{\phi_1 + (\theta(0) - \mu_1/\mu_2)/\,(\theta(0) + \mu_1/\mu_2)e^{-2kt_1}}{1 + \phi_1\,(\theta(0) - \mu_1/\mu_2)/\,(\theta(0) + \mu_1/\mu_2)e^{-2kt_1}} \tag{29}$$

$$\lambda_2 = \frac{\phi_1 + (\theta(t_2) - \mu_1/\mu_2)/\,(\theta(t_2) + \mu_1/\mu_2)}{1 + \phi_1\,(\theta(t_2) - \mu_1/\mu_2)/\,(\theta(t_2) + \mu_1/\mu_2)}. \tag{30}$$

ϕ_1, ϕ_2, and $\theta(x)$ are defined as follows:

$$\theta(x) = \left(1 - \phi_2 e^{-2kx}\right) / \left(1 + \phi_2 e^{-2kx}\right) \tag{31}$$

$$\phi_1 = \left[(\mu_1' - j\mu_1'') - 1\right] / \left[(\mu_1' - j\mu_1'') + 1\right] \tag{32}$$

$$\phi_2 = \left[(\mu_2' - j\mu_2'') - 1\right] / \left[(\mu_2' - j\mu_2'') + 1\right]. \tag{33}$$

The mutual resistance and inductance between volumetric filamentary loops are obtained from z_{gl} $(= R_{gl} + j\omega M_{gl})$, where

$$R_{gl} = \text{real}\left\{z_{gl}\right\} = \text{real}\left\{z_{gl.\text{mag}}\right\} \tag{34}$$

$$M_{gl} = M_{gl.\text{air}} + M_{gl.\text{mag}}. \tag{35}$$

$M_{gl.\text{air}}$ and $M_{gl.\text{mag}}$ are given as

$$M_{gl.\text{air}} = \text{imag}\left\{z_{gl.\text{air}}\right\}/\omega \tag{36}$$

$$M_{gl.\text{mag}} = \text{imag}\left\{z_{gl.\text{mag}}\right\}/\omega. \tag{37}$$

As eddy current effects between volumetric filamentary loops are negligible with meshes less than skin depth, R_{gl} of (34) is solely due to the losses in magnetic sheets. On the other hand, M_{gl} comprises $M_{gl.\text{air}}$ and $M_{gl.\text{mag}}$, which accounts for the increased mutual inductance by magnetic sheets.

When $g = l$ in (23), z_{gg} becomes the self–impedance of the gth volumetric filamentary loop, z_g

$$z_g = R_g + j\omega L_g \tag{38}$$

where

$$R_g = R_{g.\text{ohm}} + R_{g.\text{mag}} \tag{39}$$

$$L_g = L_{g.\text{air}} + L_{g.\text{mag}}\,. \tag{40}$$

$R_{g.\text{ohm}}$, $R_{g.\text{mag}}$, $L_{g.\text{air}}$, and $L_{g.\text{mag}}$ are given by

$$R_{g.\text{ohm}} = 2\pi r_g/(\sigma A) \tag{41}$$

$$R_{g.\text{mag}} = \text{real}\left\{z_{gg.\text{mag}}\right\} \tag{42}$$

$$L_{g.\text{air}} = \text{imag}\left\{z_{gg.\text{air}}\right\}/\omega \tag{43}$$

$$L_{g.\text{mag}} = \text{imag}\left\{z_{gg.\text{mag}}\right\}/\omega \tag{44}$$

where A of (41) is the cross-sectional area of a volumetric filamentary loop. $R_{g.\text{ohm}}$ is the resistance due to the ohmic loss in the gth volumetric filamentary loop, and it is included in (39). $R_{g.\text{mag}}$ and $L_{g.\text{mag}}$ represent the additional self-resistance, and inductance caused by lossy magnetic sheets, respectively.

III. MODEL VERIFICATION

The proposed model is verified with simulations and measurements conducted under various frequencies and geometry conditions. Using the proposed model, implemented in MATLAB, the impedances of coupled coils are calculated. Fig. 7(a) and (b) shows the photographs of the measurement setup and fabricated coils, respectively. The measurement is conducted using an LCR meter (IM 3536, Hioki). The acryl spacer is inserted between Coil #1 and Coil #2 to adjust the transfer distance, S_z (Coil #1 is located below the spacer). As shown in Fig. 7(b), copper windings ($\sigma = 5.8 \times 10^7$ S/m) are fabricated using printed circuit boards. The geometric parameters of winding patterns are listed in Table II. Two different types of nanocrystal sheets, each with dimensions of 60 mm × 60 mm and a thickness of 0.084 mm, are employed as magnetic sheet. As shown, Coil #1 and Coil #2 consist of (Winding #1 and Sheet #1) and (Winding #2 and Sheet #2), respectively, where the spaces between copper

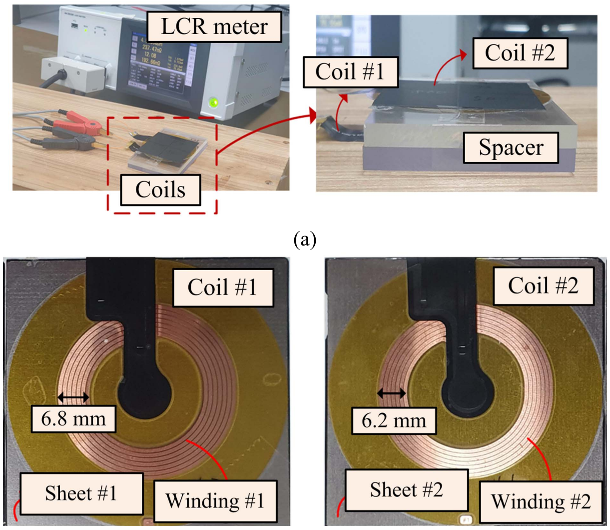

(a)

(b)

Fig. 7. Photographs of (a) measurement setup and (b) fabricated coils.

TABLE II
GEOMETRICAL PARAMETERS OF THE FABRICATED WINDINGS

Symbol	Quantity	Value
w_1, w_2	pattern width of Winding #1, #2	0.8 mm
h_1, h_2	pattern thickness of Winding #1, #2	0.1 mm
g_1	gap between patterns of Winding #1	0.2 mm
g_2	gap between patterns of Winding #2	0.1 mm
N_1, N_2	turn number of Winding #1, #2	7
R_{out1}, R_{out2}	Outer radius of Winding #1, #2	19 mm

TABLE III
SPECIFICATIONS OF MAGNETIC SHEETS

	μ	100 kHz	200 kHz	300 kHz	400 kHz
Sheet #1	μ_1'	955	935	925	910
	μ_1''	57	89	116	137
Sheet #2	μ_2'	725	720	710	700
	μ_2''	29	50	64	81

winding patterns and magnetic sheets are 0.104 mm ($d_1 = d_2 = 0.104$ mm). The specifications for Sheet #1 and Sheet #2 are listed in Table III.

Varying the frequency, the inductances and resistances of coupled coils are calculated for S_z of 2.518 mm and d of 0 mm. Fig. 8 compares the calculations with measured results. M and R_M are measured through series-aiding and series-opposing connections between windings [14], [19]. The calculated results are well aligned with measurements, validating the accuracy of the proposed analytic model.

As the frequency increases, $L_{\#1}$, $L_{\#2}$, and M decrease due to increased eddy currents within the conductive winding patterns. The reduction in inductances occurs because the direction of the induced eddy current is such that it opposes the change in the magnetic field that produced them [23].

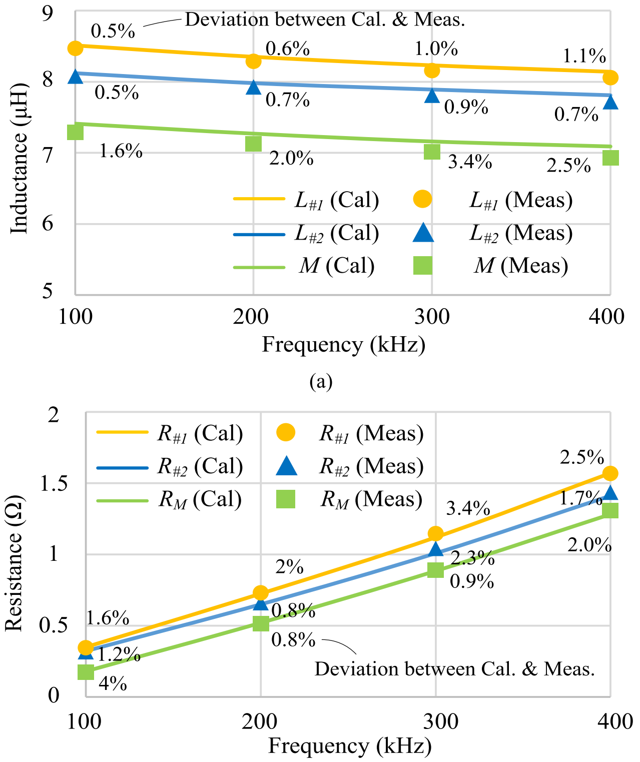

(a)

(b)

Fig. 8. Calculated and measured (a) inductances and (b) resistances with respect to the frequency when $S_z = 2.518$ mm and $d = 0$ mm.

Conversely, $R_{\#1}$ and $R_{\#2}$ increase for higher frequencies. It is also due to increased eddy currents, which exacerbate skin and proximity effects. As Winding #1 and Winding #2 mutually exert a greater influence on the ohmic loss in each other via intensified eddy current at higher frequencies, R_M increases. In addition, larger values of μ_1'' and μ_2'' lead to an increase in R_M for higher frequencies as well.

By varying S_z, the inductance and resistance of Coil #1 and Coil #2 are calculated at 100 kHz with a lateral offset of 4 mm ($d = 4$ mm). In Fig. 9, the calculated results show a good correlation with those obtained from FEM simulations and measurements. As S_z increases, inductances decrease due to the diminishing influence of magnetic sheets. Also, a larger S_z results in weakened magnetic fields around windings, thereby reducing resistances due to attenuation of the skin and proximity effects.

Calculated $R_{\#1}$ and $R_{\#2}$ are slightly lower than those of simulations and measurements. The proposed model, for efficient computing, assumes a constant current distribution along the path of a circular loop. However, in cases of misalignment, the current tends to concentrate on one side of a loop due to asymmetry, leading to slightly higher resistances than those calculated. On the other hand, the calculated R_M is slightly higher than the measured results by 4.2% to 13.3% (6–7 mΩ) because the magnetic sheets are assumed to be infinite in the radial direction for the calculation. This assumption introduces a discrepancy in the calculation for the small magnetic sheets.

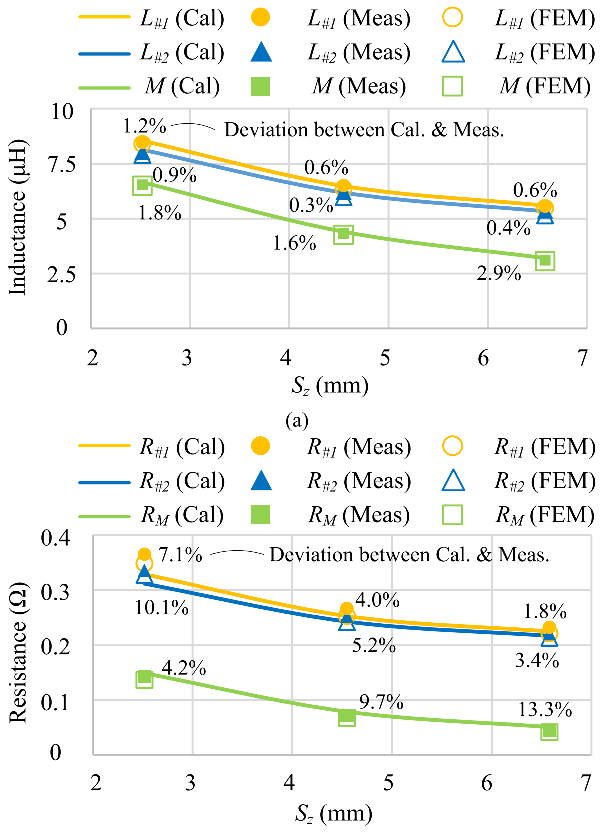

(a)

(b)

Fig. 9. Calculated, simulated, and measured (a) inductances and (b) resistance, varying S_z when $d = 4$ mm.

TABLE IV
COMPUTING TIME AND NUMBER OF MESHES

	Computing time (s)	Number of meshes
Proposal	235	112
3-D FEM	7243	2968975

To evaluate the impact of finite sheet size, experiments are conducted using various magnetic sheet dimensions. Fig. 10 shows the calculated and measured results while the sizes of Sheet #1 and Sheet #2, L_{sh}, vary from 50 to 60 mm. As expected, for smaller magnetic sheets, the calculation accuracy of the proposed model tends to decline due to the assumption about magnetic sheet sizes.

Table IV compares the computing times of a 3-D FEM simulator (Ansys Maxwell 2023) and the proposed model for S_z of 2.518 mm, d of 4 mm, and a frequency of 100 kHz. The computations are conducted using a 4-core CPU with a clock frequency of 3.9 GHz. The proposed model is around 31 times faster than the FEM simulator. In the FEM simulation, the percentage error is set to 0.2% based on the simulated and measured results. Table V compares simulated R_M with calculated and measured results with respect to the percentage error setup. For a lower percentage error, the simulated R_M approaches the measured value but the computing time increases significantly.

TABLE V
SIMULATED R_M AND COMPUTING TIME WITH RESPECT TO PERCENTAGE ERROR SETUP

	Percentage Error 1%	Percentage error 0.3%	Percentage error 0.2%
Simulated R_M	123 mΩ	129 mΩ	135 mΩ
Calculated R_M		149 mΩ	
Measured R_M		140 mΩ	
Computing time (s)	2527	4234	7243

Fig. 11 illustrates the meshes generated in an FEM simulation and the proposed model. Circular loops are replaced by polygonal loops for the efficient simulation in the FEM. The FEM simulator generates 2 968 975 meshes to achieve low convergence error, whereas the proposed model requires only 112 meshes. Because the proposed model is based on a 2-D meshing operation applied to winding patterns. Each loop of winding patterns is divided into eight volumetric filamentary loops using meshes of 0.1 mm × 0.1 mm. Furthermore, unlike FEM simulations, the proposed model does not require mesh generation for magnetic sheets, as the impacts of magnetic sheets are incorporated in (23) and (38). Utilizing fewer meshes conserves computing resources and results in more efficient calculations.

IV. ESTIMATION OF THE LOSSES

In this section, a methodology for estimating the ohmic and magnetic losses in windings and magnetic sheets is presented. For the loss estimation, the currents of volumetric filamentary loops should first be derived. When the currents of Coil #1 and Coil #2, $I_{\#1}$ and $I_{\#2}$, are given, the currents flowing through volumetric filamentary loop can be derived by solving the equivalent circuit in Fig. 4. The matrix $\boldsymbol{I_L}$ represents the currents in $(N_1 + N_2)$ loops, with its elements being $I_{\#1}$ and $I_{\#2}$, as detailed in Section II-C. $\boldsymbol{V_f}$ consists of the voltages across volumetric filamentary loops. The elements of $\boldsymbol{V_f}$ can be derived from $\boldsymbol{V_L}$. For instance, if V_p represents the voltage of the pth loop, then the voltages of volumetric filamentary loops within the pth loop (ranging from the $p_{.\min}$ to the $p_{.\max}$ filamentary loops in Fig. 4) are identical to V_p because they are connected in parallel, as illustrated in Fig. 4. Then, in (11)–(13), $\boldsymbol{I_f}$ whose elements are the currents of volumetric filamentary loops is obtained. The derivation procedure of $\boldsymbol{I_f}$ is shown in Fig. 12.

Once the currents of the volumetric filamentary loops are derived, the power losses in windings of Coil #1 and Coil #2, $P_{\text{wind}\#1}$ and $P_{\text{wind}\#2}$, are calculated as follows:

$$P_{\text{wind}\#1} = \frac{1}{2}\sum_{g\,=\,1}^{N_{T1}} R_{g.\text{ohm}}|i_g|^2 \tag{45}$$

$$P_{\text{wind}\#2} = \frac{1}{2}\sum_{g\,=N_{T1}\,+1}^{N_{T}} R_{g.\text{ohm}}|i_g|^2 \tag{46}$$

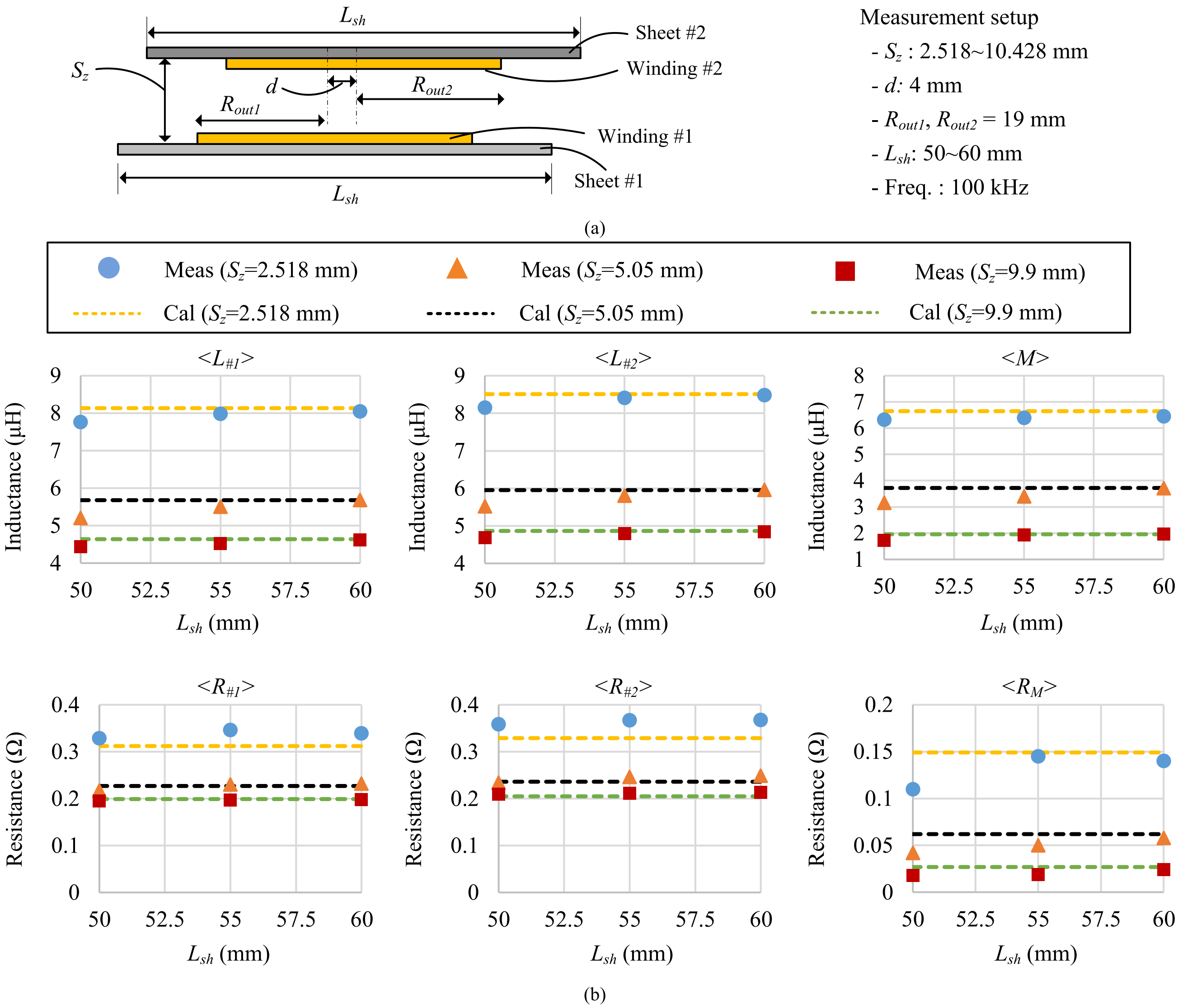

Fig. 10. Comparison of calculations and measurements for different sheet sizes, L_{sh}. (a) Measurement setup. (b) Calculated and measured results.

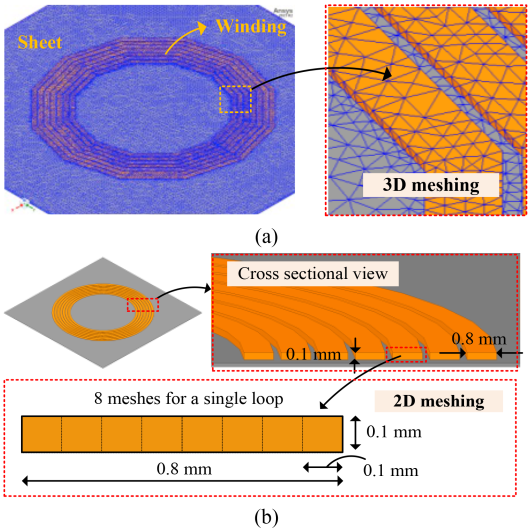

Fig. 11. Meshes of (a) an FEM simulation and (b) the proposed model.

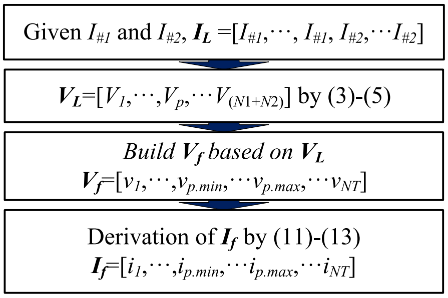

Fig. 12. Derivation of the currents of volumetric filamentary loops when coil currents, $I_{\#1}$ and $I_{\#2}$, are given.

where i_g is the gth element of $\boldsymbol{I_f}$, representing the current of the gth volumetric filamentary loop ($g = 1, 2, \ldots, N_T$), and $R_{g.\mathrm{ohm}}$ calculated in (41).

As explained, the mutual resistances between volumetric filamentary loops are solely attributable to the losses of magnetic

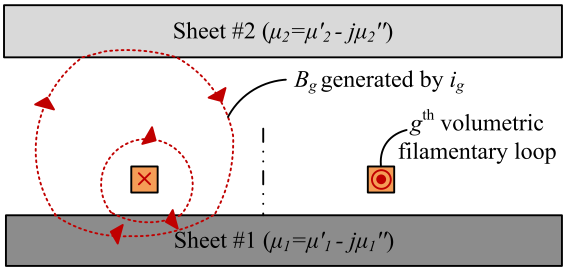

Fig. 13. Illustration of the magnetic field generated by i_g, B_g.

sheets. Therefore, the total magnetic loss, P_{mag}, is derived by

$$P_{\text{mag}} = \frac{1}{2}\sum_{k=1}^{N_T}\sum_{l=1}^{N_T} R_{gl}\text{real}(i_g i_l{}^*) \tag{47}$$

where $(\bullet)^*$ represents the complex conjugate of $(\bullet)$.

Fig. 13 illustrates the magnetic field generated by i_g, denoted as B_g. B_g flows through Sheet #1 and Sheet #2, leading to magnetic losses in both Sheet #1 and Sheet #2. Consequently, R_{gl} calculated in (34) encompassed the losses of both magnetic sheets. R_{gl} comprises $R_{gl.\#1}$ and $R_{gl.\#2}$, representing the resistances corresponding to magnetic losses in Sheet #1 and Sheet #2, respectively. To estimate the losses in each sheet, R_{gl} needs to be decomposed into $R_{gl.\#1}$ and $R_{gl.\#2}$.

To obtain $R_{gl.\#1}$, the loss of Sheet #2 can be excluded from R_{gl} by setting μ_2'' to zero, representing the absence of the loss in Sheet #2. Therefore, $R_{gl.\#1}$ is obtained by calculating R_{gl} with μ_2'' set to 0. Similarly, $R_{gl.\#2}$ can be obtained by setting μ_1'' to 0 and calculating R_{gl} from this configuration.

Then, the magnetic losses dissipated in Sheet #1 and Sheet #2 can be calculated using $R_{gl.\#1}$ and $R_{gl.\#2}$ as

$$P_{\text{mag}\#1} = \frac{1}{2}\sum_{g=1}^{N_T}\sum_{l=1}^{N_T} R_{gl.\#1}\text{real}(i_g i_l^*) \tag{48}$$

$$P_{\text{mag}\#2} = \frac{1}{2}\sum_{g=1}^{N_T}\sum_{l=1}^{N_T} R_{gl.\#2}\text{real}(i_g i_l^*). \tag{49}$$

A. Investigation of a Coil Resistance

Using the presented method, the self–resistance of Coil #1, $R_{\#1}$, is analyzed for S_Z of 2.518 mm, d of 0 mm, and a frequency of 100 kHz. With the settings of $I_{\#1} = 1$ A and $I_{\#2} = 0$ A, the total power loss, P_{total}, is calculated in (45)–(49)

$$P_{\text{total}} = P_{\text{wind}\#1} + P_{\text{wind}\#2} + P_{\text{mag}\#1} + P_{\text{mag}\#2}. \tag{50}$$

According to the resistance definition, when $I_{\#1} = 1$ A, $R_{\#1}$ is given as

$$\begin{aligned} R_{\#1} &= 2P_{\text{total}}/|I_{\#1}|^2 \\ &= R_{\#1.\text{wind}\#1} + R_{\#1.\text{wind}\#2} + R_{\#1.\text{mag}\#1} \\ &\quad + R_{\#1.\text{mag}\#2} \end{aligned} \tag{51}$$

where

$$R_{\#1.\text{wind}\#1} = 2P_{\text{wind}\#1} \tag{52}$$

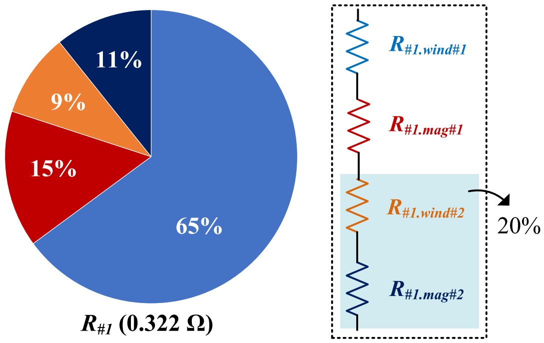

Fig. 14. Breakdown of the self–resistance of Coil #1, $R_{\#1}$.

$$R_{\#1.\text{wind}\#2} = 2P_{\text{wind}\#2} \tag{53}$$

$$R_{\#1.\text{mag}\#1} = 2P_{\text{mag}\#1} \tag{54}$$

$$R_{\#1.\text{mag}\#2} = 2P_{\text{mag}\#2}. \tag{55}$$

$R_{\#1.\text{wind}\#1}$ and $R_{\#1.\text{wind}\#2}$ represent the resistances corresponding to the ohmic losses in the Winding #1 and Winding #2, respectively, while $R_{\#1.\text{mag}1}$ and $R_{\#1.\text{mag}2}$ denote the resistances arising from the magnetic losses in Sheet #1 and Sheet #2, respectively. These elements collectively contribute to $R_{\#1}$, as illustrated in Fig. 14. Notably, the elements on the secondary side, $R_{\#1.\text{wind}\#2}$ and $R_{\#1.\text{mag}\#2}$, constitute 20% of $R_{\#1}$. Specifically, $R_{\#1.\text{wind}\#2}$ is a result of the eddy current induced in Winding #2 by $I_{\#1}$. The magnetic field generated by $I_{\#1}$ passes through Sheet #2, which causes magnetic losses in Sheet #2.

B. Loss Analysis of a WPT

For the loss breakdown analysis, Coil #1 and Coil #2 in Fig. 7 are assumed to be designated as the Tx and Rx coils, respectively. The equivalent circuit including coils, a compensation capacitor, and a load, is depicted in Fig. 15(a) for S_z of 2.518 mm, d of 0 mm, and a frequency of 100 kHz. A 4.1 Ω resistor is used as a load with a load power of 10 W. The magnitudes and phase difference of $I_{\#1}$ and $I_{\#2}$ are calculated for various values of $C_{\#2}$, as shown in Fig. 15(b). By Kirchhoff's voltage law, $I_{\#1}$ is given as

$$I_{\#1} = -\left(Z_{22} + \frac{1}{j\omega C_{\#2}} + R_L\right) \times \frac{I_{\#2}}{Z_{21}} \tag{56}$$

where the magnitude of $I_{\#2}$ remains constant at 2.21 A to maintain 10 W load power. $I_{\#1}$ is minimized when $C_{\#2} = 297$ nF, denoted by $C_{\#2.\text{res}}$, the value for resonating Coil #2.

By using (45)–(49), the loss in each component is estimated. Fig. 16(a) shows the power losses in components for different values of $C_{\#2}$. The solid and dotted lines represent the losses calculated using the proposed method. These calculated losses coincide with FEM results, thereby verifying the proposed loss estimation method. As $C_{\#2}$ increases, $P_{\text{wind}\#2}$, $P_{\text{mag}\#1}$, and $P_{\text{mag}\#2}$ decrease. As $C_{\#2}$ increases, the phase difference between $I_{\#1}$ and $I_{\#2}$, denoted by θ_d, approaches 180°. Consequently, the opposing magnetic fields generated by $I_{\#1}$ and $I_{\#2}$ mutually weaken each other. These mutual field weakening

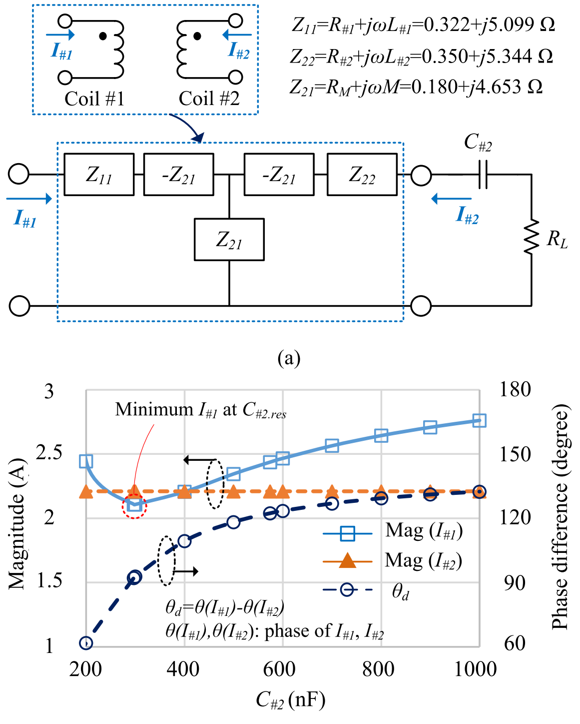

(a)

(b)

Fig. 15. (a) Equivalent circuit including a load for loss analysis. (b) Magnitudes and phase difference of $I_{\#1}$ and $I_{\#2}$ in respect to $C_{\#2}$.

effects cause the net magnetic fields incident on winding patterns to decrease, resulting in the reduced eddy current losses. These findings are consistent with the results of [8] and [11]. Furthermore, it should be noted that magnetic losses are also reduced as the net magnetic fields passing through magnetic sheets decrease. However, as $C_{\#2}$ exceeds 297 nF, $I_{\#1}$ begins to increase, leading to higher $P_{\text{wind\#1}}$, regardless of mutual field weakening effects caused by θ_d. These situations present a trade-off relation between $P_{\text{wind\#1}}$ and other losses. Due to this trade-off relation, there exists a specific value of $C_{\#2}$ that minimizes the total loss.

In Fig. 16(b), the numerically calculated total loss using (45)–(50), denoted as P_{total}, is compared with that obtained from the equation presented in [7]

$$P_{\text{total}} = \frac{1}{2}R_{\#1}|I_{\#1}|^2 + \frac{1}{2}R_{\#2}|I_{\#2}|^2 + R_M\text{real}\left(I_{\#1}I_{\#2}^*\right). \quad (57)$$

The numerically calculated P_{total} aligns well with the results of (57), validating the proposed modeling method.

P_{total} is minimized when $C_{\#2}$ is 574 nF, which coincides with the optimal value of $C_{\#2}$ for minimizing loss, $C_{\#2.\text{opt}}$, presented in [20]

$$C_{\#2.\text{opt}} = \frac{1}{\omega^2\left(L_{\#2} - M \times R_M/R_{\#1}\right)} \quad (58)$$

Importantly, $C_{\#2.\text{opt}}$ is greater than $C_{\#2.\text{res}}$, which differs from the results in [21] and [22]. This is because the referenced articles have studied loosely coupled coils and have neglected R_M in (58). Even though $I_{\#1}$ is minimized at $C_{\#2.\text{res}}$, the minimum P_{total} occurs at $C_{\#2.\text{opt}}$ due to the reduction in losses from mutual field weakening effects, which is attributed to a larger phase difference in $I_{\#1}$ and $I_{\#2}$ at higher $C_{\#2}$. R_M reflects this mutual influence of losses between coils. The analysis conducted so far indicates that adjusting coil current phases with $C_{\#2}$ effectively reduces the losses in both windings and magnetic sheet.

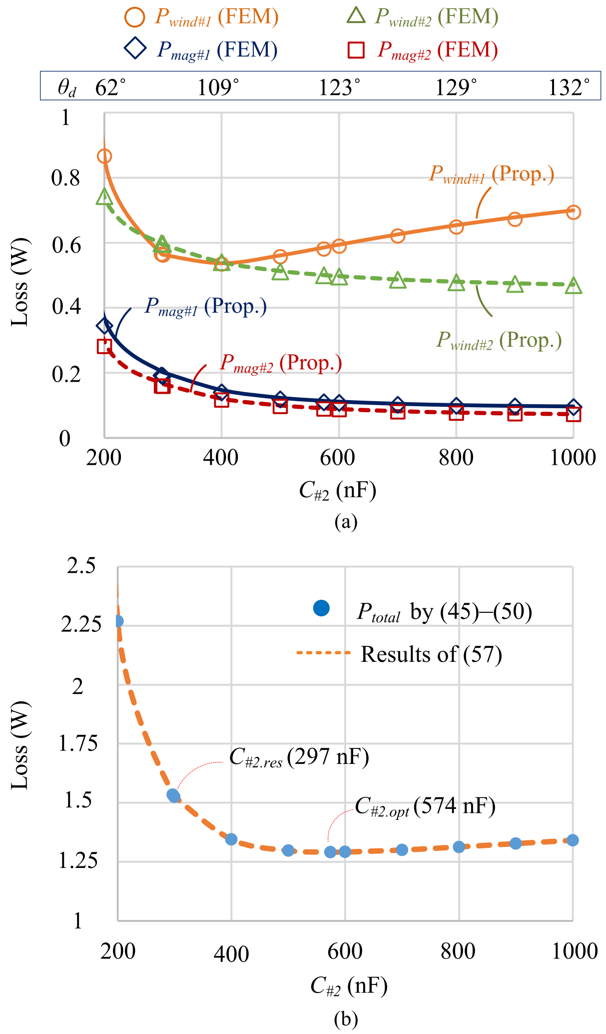

(a)

(b)

Fig. 16. (a) Estimation of losses in components. (b) Total loss for different values of $C_{\#2}$.

The results in Fig. 16(a) and (b) indicate that the losses in Coil #1 and Coil #2 should not be estimated simply by $I_{\#1.\text{rms}}^2 R_{\#1}$ and $I_{\#2.\text{rms}}^2 R_{\#2}$, respectively, where $I_{\#1.\text{rms}}$ and $I_{\#2.\text{rms}}$ represent the root mean square values of $I_{\#1}$ and $I_{\#2}$. For instance, at a $C_{\#2}$ of 574 nF, the losses in Coil #1 and Coil #2 calculated by $(P_{\text{wind\#1}} + P_{\text{mag\#1}})$ and $(P_{\text{wind\#2}} + P_{\text{mag\#2}})$, which are 0.7 W and 0.59 W, respectively. In contrast, the conventional calculation using $I_{\#1.\text{rms}}^2 R_{\#1}$ and $I_{\#2.\text{rms}}^2 R_{\#2}$ yields 0.96 W and 0.85 W, respectively, demonstrating significant discrepancies compared to the results obtained from the proposed model and FEM simulations. These discrepancies arise because $R_{\#1}$ includes the ohmic loss due to eddy current induced in Winding

#2 and the magnetic loss of Sheet #2, as shown in Fig. 9. Likewise, $R_{\#2}$ follows the same pattern of $R_{\#1}$.

In addition, in the conventional calculations of $I^2_{\#1.\mathrm{rms}}R_{\#1}$ and $I^2_{\#2.\mathrm{rms}}R_{\#2}$, the impact of the phase difference between $I_{\#1}$ and $I_{\#2}$ is not considered. However, the phases of currents significantly influence the losses of coupled coils, as explained. These observations show the limitations of conventional circuit analysis and the advantages of the proposed model in accurately dissecting power losses.

V. CONCLUSION

A precise analytic model for inductively coupled WPT with lossy magnetic sheets is suggested and validated. Skin effect, proximity effect, and mutual interaction between coils through eddy currents are captured with a PEEC-based model. By applying impedance formulas considering lossy magnetic sheets, the complex permeabilities are efficiently reflected in the analytic model. Compared with a commercial 3-D FEM simulator, the proposed model offers more efficient impedance calculation by significantly reducing the number of meshes. Furthermore, this article introduces a novel loss analysis method to estimate ohmic and magnetic losses in windings and magnetic sheets. This loss estimation method is validated through FEM simulations and corroborated by analytic results from a previous study. The analysis results indicate adjusting the phase of coil currents can reduce losses in windings and magnetic sheets, especially given the significant mutual influence between inductively coupled coils with lossy magnetic sheets. The proposed modeling and loss estimation methods can be utilized for designing wireless charging coils, such as optimizing winding geometries and selecting appropriate magnetic sheets.

REFERENCES

[1] S. Y. Hui, “Planar wireless charging technology for portable electronic products and Qi,” *Proc. IEEE*, vol. 101, no. 6, pp. 1290–1301, Jun. 2013.

[2] P. K. Chittoor, B. Chokkalingam, and L. Mihet-Popa, “A review on UAV wireless charging: Fundamentals, applications, charging techniques, and standards,” *IEEE Access*, vol. 9, pp. 69235–69266, 2021.

[3] A. Sagar et al., “A comprehensive review of the recent development of wireless power transfer technologies for electric vehicle charging systems,” *IEEE Access*, vol. 11, pp. 83703–83751, 2023.

[4] M. Haerinia and R. Shadid, “Wireless power transfer approaches for medical implants: A review,” *Signals*, vol. 1, no. 2, pp. 209–229, Dec. 2020.

[5] D.-H. Kim, S. Kim, S.-W. Kim, J. Moon, I. Cho, and D. Ahn, “Coupling extraction and maximum efficiency tracking for multiple concurrent transmitters in dynamic wireless charging,” *IEEE Trans. Power Electron.*, vol. 35, no. 8, pp. 7853–7862, Aug. 2020.

[6] R. Qin, J. Li, J. Sun, and D. J. Costinett, “Fully compensated self–resonant coil with low E–field and low profile for consumer electronics wireless charging,” in *Proc. IEEE Appl. Power Electron. Conf. Expo.*, 2023, pp. 795–802.

[7] J. E. Bracken, *Mutual Resistance in Spicelink*. Pittsburgh, PA, USA: Ansoft Corp., 2000.

[8] H. H. Cui, M. H. Kao, L. L. Xue, and K. D. T. Ngo, “Enhanced inductance and winding loss model for coupled inductors,” in *Proc. IEEE Energy Convers. Congr. Expo.*, 2020, pp. 3518–3523.

[9] K. Niyomsatian, J. J. C. Gyselinck, and R. V. Sabariego, “Experimental extraction of winding resistance in Litz–wire transformers–Influence of winding mutual resistance,” *IEEE Trans. Power Electron.*, vol. 34, no. 7, pp. 6736–6746, Jul. 2019.

[10] E. L. Barrios, D. Elizondo, A. Ursúa, and P. Sanchis, “Winding resistance measurement in power inductors–Understanding the impact of the winding resistance,” *IEEE Access*, vol. 9, pp. 92224–92238, 2021.

[11] C. Carretero, “Coupling power losses in inductive power transfer systems with Litz wire coils,” *IEEE Trans. Ind. Electron.*, vol. 64, no. 6, pp. 4474–4482, Jun. 2017.

[12] C. M. Zierhofer and E. S. Hochmair, “Geometric approach for coupling enhancement of magnetically coupled coils,” *IEEE Trans. Biomed. Eng.*, vol. 43, no. 7, pp. 708–714, Jul. 1996.

[13] W. G. Hurley and M. C. Duffy, “Calculation of self–and mutual impedances in planar sandwich inductors,” *IEEE Trans. Magn.*, vol. 33, no. 3, pp. 2282–2290, May 1997.

[14] Y. P. Su, X. Liu, and S. Y. R. Hui, “Mutual inductance calculation of movable planar coils on parallel surfaces,” *IEEE Trans. Power Electron.*, vol. 24, no. 4, pp. 1115–1123, Apr. 2009.

[15] D.-H. Kim, J. Kim, and Y.-J. Park, “Optimization and design of small circular coils in a magnetically coupled wireless power transfer system in the megahertz frequency,” *IEEE Trans. Microw. Theory Techn.*, vol. 64, no. 8, pp. 2652–2663, Aug. 2016.

[16] S. Stoecklin, A. Yousaf, G. Gidion, and L. Reindl, “Efficient wireless power transfer with capacitively segmented RF coils,” *IEEE Access*, vol. 8, pp. 24397–24415, 2020.

[17] M. Lu and K. D. T. Ngo, “Analytical calculation of proximity effect resistance for planar coil with Litz wire and ferrite plate in inductive power transfer,” *IEEE Trans. Ind. Appl.*, vol. 55, no. 3, pp. 2984–2991, May/Jun. 2019.

[18] D.-H. Kim and Y.-J. Park, “Optimization of a small planar spiral coil on a magnetic substrate for quality factor using volume filament model,” in *Proc. IEEE Wireless Power Transfer Conf.*, 2016, pp. 1–4.

[19] C. Feeney, J. Zhang, and M. Duffy, “AC winding loss of phase–Shifted coupled windings,” *IEEE Trans. Power Electron.*, vol. 31, no. 2, pp. 1472–1478, Feb. 2016.

[20] M. Zargham and P. G. Gulak, “Maximum achievable efficiency in near–field coupled power transfer systems,” *IEEE Trans. Biomed. Circuits Syst.*, vol. 6, no. 3, pp. 228–245, Jun. 2012.

[21] C.-J. Chen, T.-H. Chi, C.-L. Lin, and Z.-C. Jou, “A study of loosely coupled coils for wireless power transfer,” *IEEE Trans. Circuits Syst. II, Exp. Briefs*, vol. 57, no. 7. pp. 536–540, Jul. 2010.

[22] J. Kim, D.-H. Kim, and Y.-J. Park, “Analysis of capacitive impedance matching networks for simultaneous wireless power transfer to multiple devices,” *IEEE Trans. Ind. Electron.*, vol. 62, no. 5, pp. 2807–2813, May 2015.

[23] J. D. Jackson, *Classical Electrodynamics*, 3rd ed. Hoboken, NJ, USA: Wiley, 1925, pp. 233–234.

Do–Hyeon Kim received the B.S. degree in electrical engineering from Yonsei University, Seoul, South Korea, in 2009, and the M.S. and Ph.D. degrees in power electrical equipment information and communications engineering from the University of Science and Technology, Ansan, South Korea, in 2017.

From 2017 to 2019, he was with Incheon National University, South Korea, as a Postdoctoral Researcher. He is currently with Samsung Electronics, Suwon, South Korea.

Dr. Kim was the recipient of the 2020 Second Prize Paper Award from IEEE TRANSACTIONS ON POWER ELECTRONICS. His research interests include power conversion circuits, magnetic components, and inductive wireless power transfer.